APPLIED SCIENCES AND ENGINEERING

Wireless, wearable elastography via mechano-acoustic wave sensing for ambulatory monitoring of tissue stiffness

Chenhang Li[1]†, Heling Wang[2,3,4]†, Ziwu Song[5,6], Wei Zhang[5,7], Yuxin Pan[1], Zihao Zhao[6], Chaorui Qiu[1], Kaiping Yin[1], Mengdi Han[8], Allison Bingqing Wang[9], Haiwen Luan[8], Jiahong Li[10], Wenyuan Yan[10], Shulin Chen[11], Haixu Shen[10], Tzu-Li Liu[11], Sabrina S. M. Lee[9], Wenbo Ding[6], Yonggang Huang[4,8,10,12], John A. Rogers[8,10,11,12,13]*, Changsheng Wu[5,7,14,15]*, Xiaoyue Ni[1,16]*

Assessing the mechanical properties of soft tissues holds broad clinical relevance. Advances in flexible electronics offer possibilities for wearable monitoring of tissue stiffness. However, existing technologies often rely on tethered setups or require frequent calibration, restricting their use in ambulatory environments. This study introduces a mechano-acoustic wave sensing technology for automated, wireless elastography. The patch-form sensor maintains conformal contact with the skin, regardless of body motion or deformation. It provides continuous, depth-sensitive estimation of subcutaneous tissue stiffness through real-time surface wave dispersion analysis. Theoretical and experimental investigations on phantom materials and tissues spanning a wide range of Young's modulus (in kilopascals to megapascals) demonstrate the capability of the device to rapidly and robustly evaluate the stiffness at depths up to several centimeters. The device shows compatibility with various tissue models, with results consistent with in-parallel ultrasound elastography measurements. Deployment of the device during exercises confirms its viability for ambulatory monitoring, enabling continuous assessment of variation in tissue stiffness.

INTRODUCTION

The biomechanics of peripheral tissues, spanning from the skin to subcutaneous layers (*1*), are critical to understanding disease progression (*2*, *3*) and guiding therapeutic strategies (*4*–*6*). Technologies that enable noninvasive or minimally invasive access to these tissues hold transformative potential for advancing biomedical research and clinical care (*7*, *8*). Longitudinal monitoring of tissue stiffness offers a means to track pathological changes over extended periods, with applications under conditions such as systemic sclerosis (*9*, *10*), hypertrophic scarring (*11*), wound healing (*12*), and peripheral edema (*13*, *14*). These insights are invaluable for evaluating disease progression and tailoring treatment strategies under chronic conditions such as skin and breast cancer (*15*–*19*). In contrast, continuous monitoring provides real-time, high-frequency measurements, allowing dynamic assessments of tissue biomechanics. This approach is particularly valuable for capturing muscle dynamics in neurological disorders such as Parkinson's disease (*20*, *21*), stroke (*22*–*24*), and cerebral palsy (*25*, *26*), where real-time feedback informs personalized interventions and rehabilitation (*22*, *27*). Beyond clinical applications, continuous stiffness monitoring supports fatigue management (*28*, *29*), injury prevention (*30*, *31*), and performance optimization in sports science (*32*–*34*). Moreover, wearable assistive robotics, such as portable exosuits, leverage real-time stiffness data to optimize torque control and modulate tissue forces for enhanced functionality (*35*, *36*).

Despite the clear benefits of longitudinal and continuous monitoring of tissue stiffness, existing noninvasive technologies face notable limitations in practical ambulatory applications. Traditional systems for quantitative assessment of tissue mechanics are often bulky or tethered, requiring manual operation or frequent calibration, thereby limiting patient mobility and long-term usability (*37*–*40*). Recent advancements in wearable technologies have begun addressing these issues by enabling skin-integrated sensing of tissue mechanics and acoustics (*41*–*49*). These innovations include miniaturized devices that use vibrational mechanics to assess the stiffness of superficial tissues (<1 cm in depth) (*41*–*43*, *47*). Devices probing wave mechanics have further expanded the sensing capability to deeper tissues (>1 cm) (*44*–*46*). For example, wearable inertial measurement units (IMUs) that measure shear wave propagation in tendons can gauge stiffness variations (*44*). Stretchable or bioadhesive ultrasound arrays have enabled wearable shear wave elastography (SWE), allowing for modulus mapping of deep tissues (*45*, *46*). Despite these advancements, the usability of wearable technologies for monitoring in naturalistic settings remains limited by system complexity, cost, and power consumption. These limitations underscore the need for low-profile wearable systems specifically designed to

---

[1]Department of Mechanical Engineering and Material Science, Duke University, Durham, NC 27708, USA. [2]Laboratory of Flexible Electronics Technology, Tsinghua University, Beijing 100084, China. [3]Institute of Flexible Electronics Technology of THU Zhejiang, Jiaxing 314000, China. [4]Department of Civil and Environmental Engineering, Northwestern University, Evanston, IL 60208, USA. [5]Department of Materials Science and Engineering, National University of Singapore, Singapore 117575, Singapore. [6]Shenzhen International Graduate School, Tsinghua University, Shenzhen 518055, China. [7]Institute for Health Innovation and Technology, National University of Singapore, Singapore 117599, Singapore. [8]Querry Simpson Institute for Bioelectronics, Northwestern University, Evanston, IL 60208, USA. [9]Department of Physical Therapy and Human Movement Sciences, Northwestern University, Chicago, IL 60611, USA. [10]Department of Material Science and Engineering, Northwestern University, Evanston, IL 60208, USA. [11]Department of Biomedical Engineering, Northwestern University, Evanston, IL 60208, USA. [12]Department of Mechanical Engineering, Northwestern University, Evanston, IL 60208, USA. [13]Department of Neurological Surgery, Feinberg School of Medicine, Northwestern University, Chicago, IL 60611, USA. [14]The N.1 Institute for Health, National University of Singapore, Singapore 117456, Singapore. [15]Department of Electrical and Computer Engineering, National University of Singapore, Singapore 117583, Singapore. [16]Department of Biostatistics and Bioinformatics, Duke University, Durham, NC 27710, USA.
*Corresponding author. Email: jrogers@northwestern.edu (J.A.R.); cwu@nus.edu.sg (C.W.); xiaoyue.ni@duke.edu (X.N.)
†These authors contributed equally to this work.

meet the demands of ambulatory monitoring of tissue stiffness, balancing performance, efficiency, and practicality.

Here, we introduce a wireless mechano-acoustic wave (MAW) sensing system for wearable elastography, addressing the limitations of existing technologies. This device leverages a mechano-acoustic sensing platform (*49–52*) optimized for intimate skin interfaces to deliver robust measurements in ambulatory settings. The device uses a pair of microelectromechanical systems (MEMS)-based IMUs to detect broadband (<800 Hz) elastic waves generated by a skin-mounted vibration actuator, with an automated algorithm performing spectral analysis of surface waves to calculate depth-dependent stiffness from measured dispersion relations. A unique feature of this approach is the ability to measure spatially averaged tissue stiffness in ambulatory settings, where real-time feedback is prioritized over resolving localized tissue heterogeneities, significantly reducing data acquisition and computational demands. Key advancements include (i) a wireless, skin-interfaced MAW sensing system; (ii) a signal processing algorithm for dispersion analysis of on-body surface waves; (iii) a mechanical model and a scaling law linking tissue stiffness to surface wave speeds in bilayer structures; and (iv) an automated pipeline for calculating bilayer stiffness, streamlining the operational process for ambulatory monitoring. The system has been demonstrated to effectively track the local stiffness variation in synthetic tissue, monitor the softening of porcine tissues upon the injection of phosphate-buffered saline (PBS) solution, and detect the stiffening of human skeletal muscles during physical exercises. This transformative platform offers promising applications in medicine, rehabilitation, and sports science, paving the way for longitudinal or continuous tissue monitoring in dynamic environments.

RESULTS

Device design and working principle

Figure 1A shows the overall MAW sensing setup consisting of a MAW sensor (weight, 4.9 g) and a disk-shaped speaker-type vibration actuator (ASX02604-R, PUI Audio; diameter, 26.5 mm; weight, 10 g; see Materials and Methods). Figure 1B presents an exploded view illustration of the MAW sensor. The circuit uses a flexible printed circuit board (fPCB; AP7164R, DuPont) composed of a middle polyimide layer (75 μm in thickness) sandwiched by patterned copper traces (18 μm in thickness). The key electronic components of the sensor include (i) two digital IMUs (MPU9250, InvenSense) for sensing skin vibrations; (ii) a flash memory (W25Q128, Winbond) for on-board data storage; (iii) a radio frequency system on chip (nRF52832, Nordic Semiconductor) for data acquisition, control, and wireless communication through Bluetooth low-energy protocols; and (iv) a rechargeable 60-mA·hour lithium-ion polymer battery for power supply. Two serpentine interconnects electrically join the two IMUs on separate fPCB islands with other components on the main board, while attenuating mechanical disturbances from the connection (fig. S1). A thin (0.5 mm) silicone elastomer shell (Silbione RTV 4420, Elkem; part A and part B, mixed with 3% of Silc Pig white silicone dye) provides a soft and waterproof encapsulation for the electronics. The fabrication process follows the methods outlined in (*36*). Figure 1C shows that the device maintains its functionality under different modes of mechanical loading, including stretching (global strain, $\varepsilon \leq 10\%$), bending (radius of curvature, $R \geq 22$ mm), and twisting (angle, $\theta_{\text{twist}} \leq 120°$). Finite element analysis (FEA) confirms that the maximum principal strains in the copper layer remain within the yielding limit (0.3%) under all loading conditions (Fig. 1D and note S1). FEA also verifies that the interfacial stresses between the device and the skin under 10% stretching stay below human sensation threshold (~20 kPa) (*49*) (fig. S2).

The MAW sensing combines the vibration actuator and the MAW sensor to induce and measure the propagation of MAWs at the surface of body. The two umbilical IMUs are positioned at a distance, $D = 20$ mm, apart (center-to-center distance gauged by a ruler) to balance phase sensitivity and signal attenuation (fig. S3 and note S2). They record vibrations at a sampling frequency of 1600 Hz, with a dynamic range of $\pm 8g$ ($g = 9.8$ m/s^2) and a digital resolution of 14 bits. A calibration experiment measures and corrects a constant time delay (~0.6 ms) between the data acquisition of the two IMUs to ensure synchronization of the clock (fig. S4 and note S3). The actuator, mounted in line with the IMUs for generating a broadband wave, is 25 mm away from the closest accelerometer (center-to-center distance gauged by a ruler) to strike the balance between minimizing damping and reducing the near-field effects caused by the interference of pressure waves (*53*, *54*) (fig. S5 and note S4). This placement ensures that the generated surface waves reach both IMUs as a coherent, unidirectional wavefront. A Bluetooth receiver (Soundsync A3352, Anker) transmits an audio signal to the actuator via an audio cable to generate vibrations (fig. S6). The signal consists of superposed sinusoidal waves with frequencies, f, ranging from 50 to 800 Hz at intervals of 10 Hz, with amplitudes scaled by $1/f$ to produce a broadband wave using lower-energy excitation. The output sound pressure level is 56 dB when measured at a distance of 10 mm from the device.

Figure 1E is a block diagram outlining the operational flow of the system. A smartphone with a customized application connects to the MAW sensor and vibration actuator for wireless control and data transfer via Bluetooth. An automated algorithm on a server computes the frequency-dependent phase velocity of the broadband wave excited from the vibration actuator and then estimates the tissue stiffness from the dispersion relation using a scaling law derived from FEA predictions. This integrated hardware and software enables real-time, ambulatory monitoring of tissue stiffness for potential applications in early diagnosis, physiotherapy, rehabilitation, and wearable robotics, etc.

Spectral analysis of surface waves on bilayer phantom materials

Human tissues typically exhibit complex, layered structures, with varying thicknesses and diverse elastic properties (*1*). Figure 2A provides an example cross-sectional illustration of a bilayer tissue model consisting of a top skin-fat layer (modulus range of 10^1 to 10^3 kPa) and a bottom muscle-organ layer (modulus range of 10^0 to 10^3 kPa) (*1*, *55*). Figure 2B shows the MAW sensing setup on a bilayer phantom material, designed to mimic a variation of skin-fat (layer 1) and muscle-organ (layer 2) tissue structures for testing. The study includes 19 phantom materials (M1 to M19) (note S5 and tables S1 and S2). Each material consists of two stacked layers of silicone elastomers in a disk shape with the same diameter ($d = 140$ mm). These layers have a similar mass density, represented by the average nominal value $\rho_0 = 1.06$ g/cm^3, and a similar Poisson's ratio ($\nu_0 = 0.5$) but differ in Young's modulus, E_i, and thickness, h_i, where the subscript, $i = 1$ and 2, denotes layer i. M1 to M10 have different layer 1 ($E_1 = 88$ to 1400 kPa, $h_1 = 9.0$ to 11.8 mm) but the same layer 2 ($E_2 = 88$ kPa, $h_2 = 80.0$ mm). M11 to M19 have the same

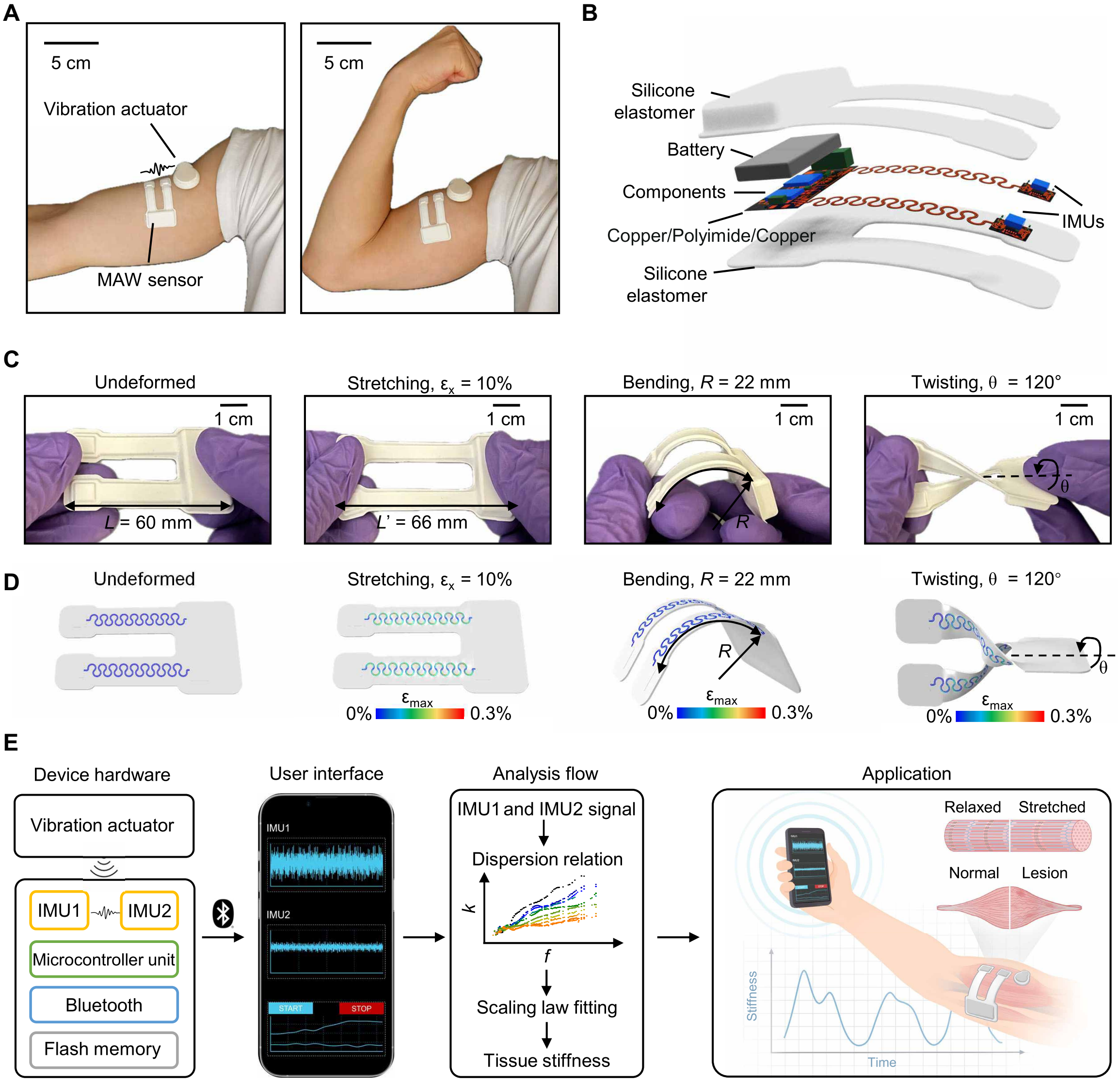

Fig. 1. Wearable MAW sensing technology. (**A**) Optical images of the MAW sensor and actuator placed on the bicep of a healthy male. (**B**) Exploded schematic of the sensor components. (**C**) Optical images of the sensor under different mechanical loading conditions. (**D**) FEA simulations showing the maximum principal strain distribution in the Cu layer under each loading condition. (**E**) Functional block diagram of the wireless MAW sensing system, illustrating the device hardware, user interface, analysis flow, and application scenarios.

layer 1 ($E_1 = 205$ kPa, $h_1 = 9.8$ mm) but different layer 2 ($E_2 = 88$ to 732 kPa, $h_2 = 9.8$ to 10.5 mm). Figure 2C shows a sample 0.5-s z-axis (vertical to the surface) acceleration data acquired from a representative bilayer phantom material, M2 ($E_1 = 166$ kPa, $h_1 = 9$ mm; $E_2 = 88$ kPa, $h_2 = 80$ mm), with and without actuation. In Fig. 2D, power spectral analysis of the data in the frequency range of interest shows that the typical noise floor is ~2.5×10^{-4} $g/\text{Hz}^{1/2}$, and the average signal-to-noise ratio of the far-end IMU is 22 dB. A discrete cross-spectral analysis of the two IMUs' measurements provides the frequency-dependent, unwrapped phase lag $\Delta\phi(f_n)$, with a coherence threshold of 0.8 applied to filter out noisy components (Fig. 2E, figs. S7 to S9, and note S3). The signal segment length ($\Delta T = 10$ s) and the averaging Hanning window size ($w = 2$ s) used in the spectral analysis determine the temporal and frequency resolution as ΔT and $1/w$ (figs. S10 to S12). Figure 2F shows the dispersion relation of the measured surface wave, i.e., the frequency-dependent wave number

$$k(f_n) = \frac{\Delta\phi(f_n)}{D} \tag{1}$$

given known, unchanged D. The penetration depth of the surface wave, $d_p(f_n)$, can be approximated as $\lambda(f_n)/3$, where λ is the wavelength (*56*). Given the excited frequency range (50 to 800 Hz) and the modulus range of the target materials (in kilopascals to megapascals), the estimated measurement depth ranges from few millimeters to several centimeters (fig. S13). The frequency-dependent surface wave speed, $C_R(f_n) = f_n/k(f_n)$, depends on the elastic properties of the dispersive media.

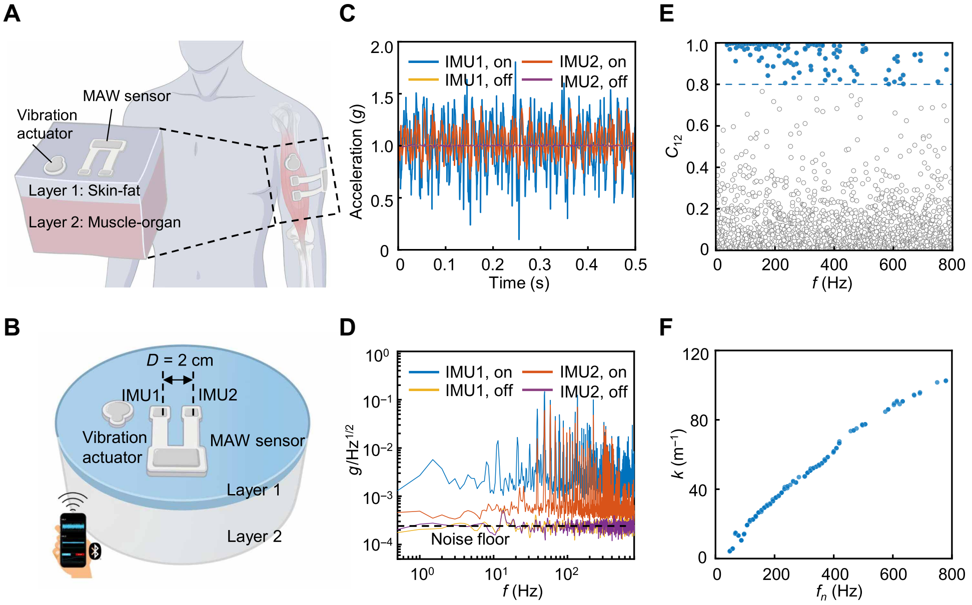

Fig. 2. MAW sensing on bilayer materials. (**A**) Schematic illustration of subcutaneous tissue modeled as a bilayer structure (skin-fat and muscle-organ). (**B**) Schematic illustration of the MAW sensor and vibration actuator placed on a bilayer phantom. (**C**) Representative 0.5-s raw data (z-axis acceleration) with actuation on and off. (**D**) Power spectral density of 10-s raw data with actuation on and off. (**E**) Coherence (C_{12}) of the signals from two IMUs, with a threshold of 0.8 applied to filter out uncorrelated noise. (**F**) Computed dispersion curve, showing wave number (k) versus frequency (f_n), with the coherence threshold applied.

A mechanical model relating MAW measurement to material stiffness

FEA provides a mechanical model to derive stiffness of a bilayer material from the dispersion relation (note S1). Figure 3A presents the FEA-predicted snapshots of z-axis (perpendicular to the surface) displacement in a phantom material (M2) as a surface wave, induced by sinusoidal point force at a frequency of 100 or 400 Hz, propagating along the x axis (parallel to the surface). Infinite boundaries eliminate reflections for simplicity (figs. S14 to S16 and note S6). A spatial Fourier analysis computes the wave number and, hence, the surface wave speed at different actuation frequencies (Fig. 3B and note S3). Figure 3C shows the experimentally measured dispersion curves from M1 to M10 in close agreement with the FEA predictions, with a root mean square error of 10% (fig. S17 and note S7). Assuming isotropic, homogeneous, and nonviscous characteristics of each layer, the shear wave speed (SWS), c_i, depends on the elastic properties of the material as (*57*)

$$c_i = \sqrt{\frac{E_i}{2\left(1+\nu_i\right)\rho_i}} \tag{2}$$

Assuming the same mass density and Poisson's ratio for each layer ($\rho_i = \rho_0$, $\nu_i = \nu_0$), dimensional analysis (*58*) using the FEA-derived dispersion relation establishes a scaling law

$$\frac{C_\mathrm{R}}{c_1} = F\left(\frac{fh_1}{c_1}, \frac{c_1}{c_2}\right) \tag{3}$$

which relates the nondimensional surface wave speed, C_R/c_1, to the nondimensional frequency, fh_1/c_1, and the ratio of SWS, c_1/c_2 (fig. S18). Figure 3D shows the FEA-predicted relationship between C_R/c_1 and fh_1/c_1 with a range of c_1/c_2. At sufficiently high frequencies, the surface waves have wavelengths significantly smaller than h_1 and penetrate only the top layer, therefore exhibiting characteristics resembling those in a homogenous material (*58*). As shown by FEA, when $f \geq f_\mathrm{th}$, where f_th is the threshold frequency dependent on the limit of nonleaky branch (fig. S19 and note S8), C_R/c_1 approaches an asymptote (*57*)

$$r_0 = \frac{0.862 + 1.14\nu_0}{1+\nu_0} \tag{4}$$

The asymptotic relationship allows for the estimation of c_1 from averaging the experimentally measured surface wave velocities $[C'_\mathrm{R}(f_n);\ n = 1, 2, \ldots, N]$ as

$$c_1 = \left\langle \frac{C'_\mathrm{R}\left(f_n\right)}{r_0} \mid f_n \geq f_\mathrm{th} \right\rangle \tag{5}$$

where $f_\mathrm{th} = f_N - 100$ Hz serves as an empirical threshold for high-frequency approximation (fig. S20 and note S8). Lower-frequency waves penetrate deeper below the bilayer interface, and the wave characteristics become nontrivial and more susceptible to boundary effects (note S6). Data points at frequencies where $d_\mathrm{p}(f_n) > d_\mathrm{max}$ are excluded, where d_max represents the maximum depth of the soft material. Then, minimizing the mean square difference between experimental measurement (C'_R) and theoretical prediction (C_R) at all frequencies yields an estimation of h_1 and c_2, as

$$h_1, c_2 = \arg\min\left(\left\langle \left[C'_\mathrm{R}\left(f_n\right) - C_\mathrm{R}\left(h_1, c_2 \middle| f_n, c_1\right)\right]^2 \right\rangle\right) \tag{6}$$

FEA simulations reveal that the sensing sensitivity, estimated by the dependence of C_R on c_2, decreases as h_1 increases (fig. S21 and note S9). To account for experimental variability, Monte Carlo simulations quantify the uncertainties in c_1, c_2, and h_1, yielding 95% confidence interval of 6, 17, and 16.5%, respectively (figs. S22 and S23 and note S7).

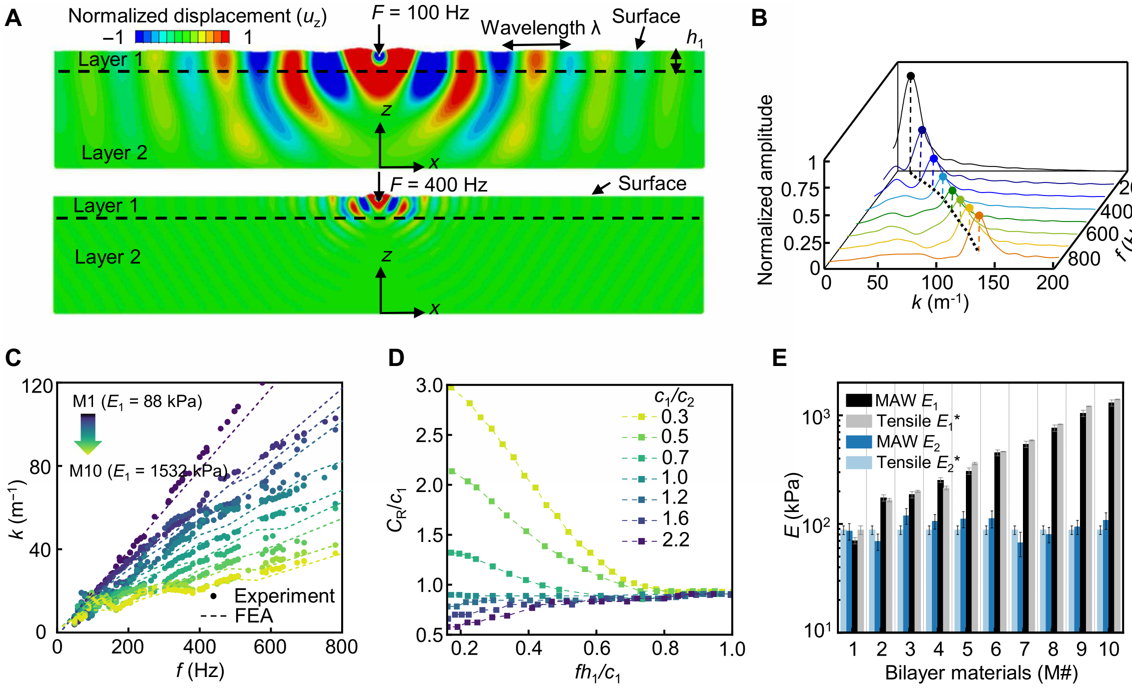

Fig. 3. A scaling model of the dispersion relation for stiffness estimation. (**A**) FEA-predicted snapshots of *z*-axis displacement in a bilayer material excited by a periodic point force along the *z* axis at frequencies of 100 or 400 Hz. (**B**) Spatial Fourier transform of the FEA-predicted *z*-axis displacement over frequencies ranging from 100 to 800 Hz (note S4). (**C**) MAW-measured and FEA-predicted dispersion curves for 10 different bilayer phantom materials with the same layer 2 but different layer 1 compositions (M1 to M10). (**D**) Scaling law derived from FEA results, relating the nondimensional surface wave speed (C_R/c_1) to the nondimensional frequency (fh_1/c_1), with the ratio of SWS (c_1/c_2) varying from 0.3 to 2.2. (**E**) Comparison of MAW-estimated Young's modulus (E_1, E_2) of the bilayer phantoms with tensile test measurements (E_1^*, E_2^*). The error bars for E_1 and E_2 are uncertainties assessed from Monte Carlo simulation, and the error bars for E_1^* and E_2^* are ±1.96 × SD from five tensile tests (note S7).

After obtaining c_i, one can estimate E_i as $2(1 + \nu_0)\rho_0 c_i^2$ from Eq. 2. Figure 3E and figs. S24 and S25 show that the MAW-measured E_1, E_2, and h_1 for M1 to M19 are comparable to the ground-truth values obtained from tensile tests and caliper measurements (E_1^*, E_2^*, and h_1^*; see Materials and Methods), with 90% of the relative difference within 18% (fig. S26). MAW sensing maintains accuracy under deformation and motion, exhibiting SWS deviations of <9% during bending (surface curvature radius, 50 to 100 mm) or uniaxial stretching (5 to 20% engineering strain along the parallel and perpendicular directions relative to the sensor orientation) and <5% under mechanical vibrations (frequencies, 3 to 7 Hz; all with amplitude, ±0.25*g* *x* axis, ±0.15*g* *y* axis, and ±0.2*g* *z* axis) (figs. S27 and S28 and note S10).

Tests on synthetic and porcine tissues

Measurements on synthetic tissues, conducted in comparison with SWE (ACUSON Sequoia, 18 L6 transducer, Siemens; see Materials and Methods), demonstrate the utility of the sensing method in analyzing biomaterials with layered structures. A benchmark test shows that the MAW- and SWE-measured SWSs are within 10% difference (fig. S29 and note S11). An artificial tissue analog (Abdominal Tissue Plate, SynDaver) featuring multilayer structures serves a skin-fat and muscle-organ tissue model. Figure 4 (A and B) shows the side view of the experimental setup, with the projected region of interest for ultrasound B-mode imaging and SWE analysis. The white dashed line at the depth of 3.7 mm visually guides the interface between the top skin-fat and underneath muscle layers. The average SWS obtained from SWE in the two layers are $c_1^* = 3.0 \pm 0.5$ m/s and $c_2^* = 3.6 \pm 0.3$ m/s, respectively. The MAW-measured SWS are $c_1 = 2.9 \pm 0.2$ m/s and $c_2 = 4.1 \pm 0.7$ m/s (Fig. 4D), with an estimated thickness of the skin layer, $h_1 = 3.6 \pm 0.6$ mm. Carving out a small plate area (10 mm by 10 mm) in the cutis of tissue analog (1 mm in thickness) and filling it with phantom materials with different modulus ($E_{\mathrm{nominal}} = 55$ kPa to 1 GPa, $c_{\mathrm{nominal}} = 4.2$ to 527 m/s) serve as a simple model for skin lesions (Fig. 4C and fig. S30) (*10*, *59*). MAW sensing distinguishes the embedment of materials with increasing stiffness through dispersion analysis (Fig. 4D, figs. S30 and S31, and note S12), by measuring slightly increasing c_1, while c_2 remains relatively unchanged. Note that the derived c_1 does not match the nominal values of the replaced material, likely due to the failure of the homogeneous layer model to describe the scenario with the presence of the discontinuous material interface.

Porcine tissue with weight-controlled injection of PBS provides an edema model. Figure 4E shows the measurement setup on a 530-g skinless pork tissue. The region below the sensor has a 4.1-mm-thick fat layer on top of a muscle layer. Following each incremental needle injection of 2-g PBS into the muscle layer, positioned 7 mm below the sensor, and after 30-s diffusion, MAW sensor and SWE acquire the SWS measurements in sequence. The zoom-in images show the boxed region of interest for ultrasound B-mode imaging and SWE analysis. Figure 4F shows the dispersion curves measured from the MAW sensor in one test. Upon a single-point needle injection of 0, 2, 4, and 6 g of PBS, SWE shows that the SWS of the top fat layer c_1^* (averaged over the depth range of 0 to 5 mm) stays relatively stable

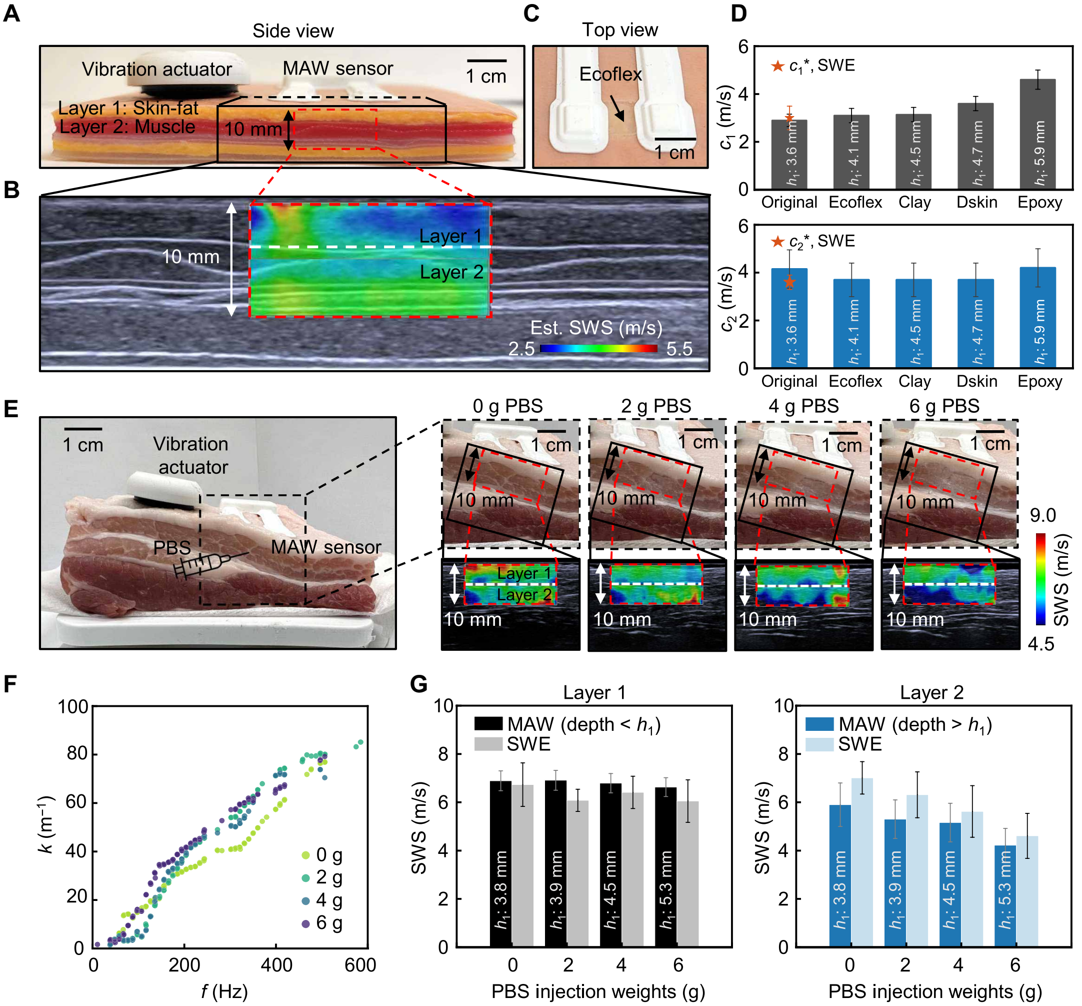

Fig. 4. MAW sensing on synthetic and porcine tissues. (**A**) Cross-sectional view of the experimental setup for MAW sensing on a multilayer synthetic tissue. (**B**) Ultrasound B-mode image overlaid with SWE analysis of the original tissue underneath the sensor. (**C**) Top view of the setup, with the top layer replaced by a slab material to simulate skin lesions. (**D**) MAW-estimated SWSs (c_1, c_2) of the original synthetic tissue, compared with the SWE measurement (c_1^*, c_2^*) and after replacement of materials with different stiffness. The error bars for c_1 and c_2 are uncertainties assessed from Monte Carlo simulation (note S7), and the error bars for c_1^* and c_2^* are ±SD of the SWS within the region of interest of SWE. (**E**) Optical images of the experimental setup and corresponding ultrasound B-mode images overlaid with SWE analysis of a 530.2-g porcine tissue after incremental injections of PBS. (**F**) Dispersion curves obtained from MAW sensing after incremental injections of PBS. (**G**) Estimated SWSs from MAW sensing (c_1, c_2) and SWE measurements (c_1^*, c_2^*). The error bars for c_1 and c_2 are uncertainties assessed from Monte Carlo simulation (note S7), and the error bars for c_1^* and c_2^* are ±SD of the SWS within the region of interest of SWE.

around a mean value of 6.32 m/s, while c_2^* (averaged over the depth range of 5 to 10 mm) decreases from 7.0 ± 0.7 to 4.6 ± 0.9 m/s as the underneath muscle layer softens with increasing level of water content (Fig. 4G). The SWS measured from the MAW sensor (c_1 and c_2) agree with the SWE results within 15% difference. The estimated top layer thickness (h_1) varies between 3.8 and 5.3 mm, marking the depth of the greatest bilayer stiffness contrast.

Ambulatory monitoring of tissue stiffness on human body

Assessing stiffness of skeletal muscles under varying loads in 11 healthy participants (7 males and 4 females, aged 24 to 47) provides a demonstration of the ambulatory monitoring capability of the MAW sensor. Figure 5 shows results from one representative participant (male, aged 28). The test starts with the participant seated quietly on a chair, wearing a MAW sensor and an actuator on the right bicep along the muscle fibers and positioning the right arm with its elbow resting on the table at a fixed angle of 60° (Fig. 5A and see Materials and Methods). The participant then holds flat objects of varying weights (0 to 4533 g) to modulate the muscle loading. Figure 5B shows the dispersion curves measured with 16 different weights from a single test on the right arm. Figure S31 includes the complete set of measurements. Figure 5C shows the average SWS ($c_{i,\mathrm{left/right}}$) from five tests conducted on the left and the right biceps over 2 days, with 10-hour intervals between each test. Here, c_1 and c_2 reflect the stiffness of the superficial skin-fat layer and deeper muscle tissue, respectively. As the weight increases, $c_{2,\mathrm{right}}$ and $c_{2,\mathrm{left}}$ exhibit an increasing trend from 2.2 and 2.6 (0 g) to 8.2 and 6.5 m/s (4533 g), indicating a stiffening of the muscle layer. Meanwhile, $c_{1,\mathrm{right}}$ and $c_{1,\mathrm{left}}$ show no clear correlation with the load at light weights (<1 kg) but exhibit a similar increasing trend at

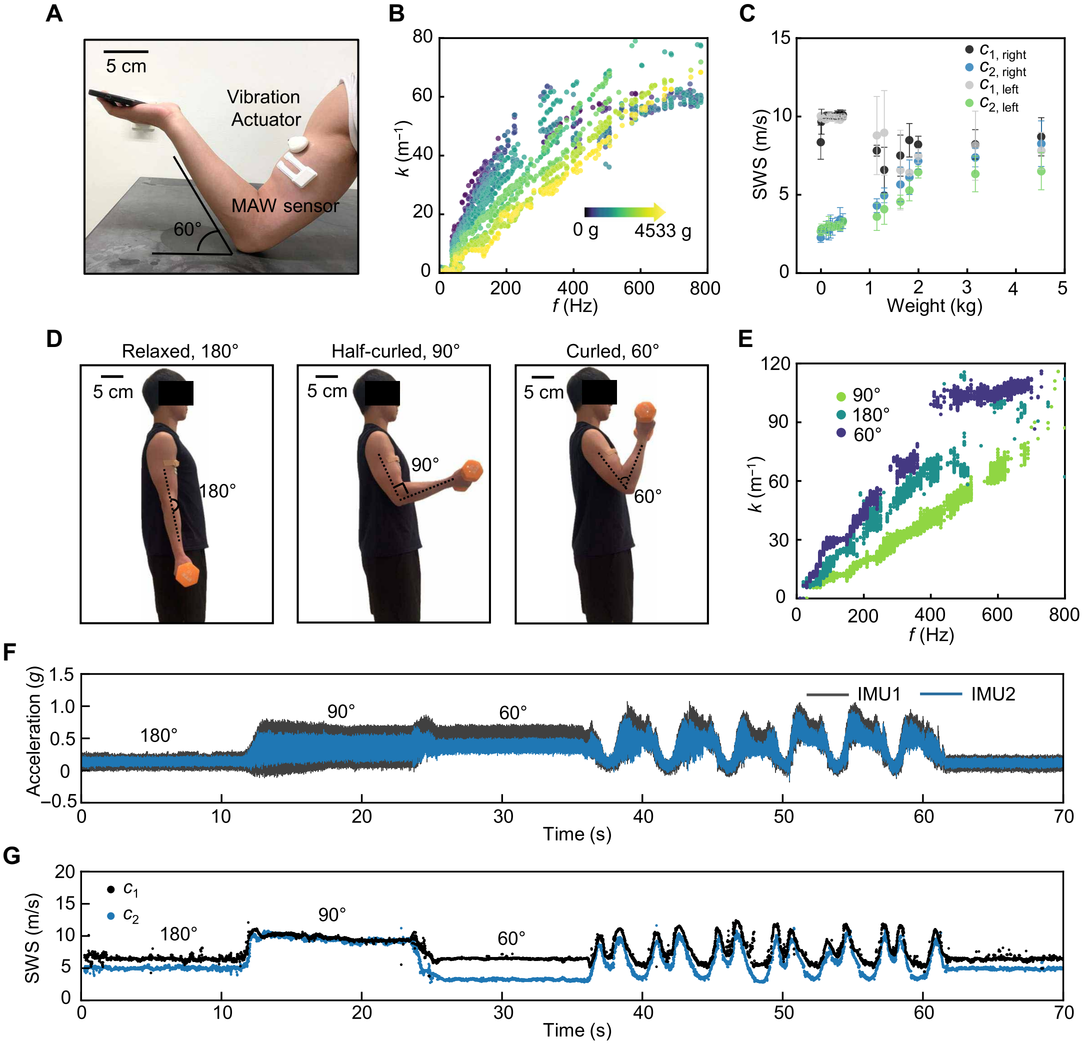

Fig. 5. MAW sensing on the human body. (**A**) Optical image of the experimental setup on a healthy male participant wearing a MAW device and a vibration actuator on the bicep while holding a flat object (240 g). (**B**) Dispersion curves obtained from a single MAW measurement as the participant holds different weights (0 to 4533 g). (**C**) Estimated SWSs from the left bicep ($c_{1,\mathrm{left}}$, $c_{2,\mathrm{left}}$) and the right bicep ($c_{1,\mathrm{right}}$, $c_{2,\mathrm{right}}$). Error bars are 1.96 × SD from five measurements taken at different times over 2 days. (**D**) Optical images of the same participant lifting a 10-lb (4533 g) dumbbell at three benchmark positions (180°, 90°, and 60°). (**E**) Superimposed dispersion curves measured from MAW sensing at each benchmark position. (**F**) Raw acceleration data recorded during a bicep-curl exercise. (**G**) Calculated SWSs synchronized with the raw acceleration data.

heavier weights (>1 kg). The sensor, with its potential to scale up to an IMU array, also demonstrates promise in measuring directional anisotropy in stiffness. In the same test, adding a sensor oriented approximately orthogonal to the original one reveals that the SWS increases rapidly in the direction along the muscle fibers while remaining relatively constant in the orthogonal direction. The observation is consistent with the expected anisotropic stiffening of muscle during isometric contraction (*60*, *61*) (fig. S32 and note S12).

Tests during physical exercises, involving substantial body movements and skin deformation, demonstrate the real-time monitoring capability of the MAW sensor. The bicep-curl exercise offers a controlled, physiologically defined model with localized and reversible modulation of deep tissue stiffness, enabling direct assessment of dynamic sensing performance. Figure 5D shows the same participant wearing a device on the right bicep while performing a bicep-curl exercise (see Materials and Methods). The participant lifted a 10-lb (4533 g) dumbbell in the right hand with the palm facing forward and the elbow angle cycling through three reference positions: straight (180°), half-curled (90°), and fully curled (60°). At all positions, the maximum change in D is 3.5%, which can contribute to a maximum error of 3.5% in the estimation of SWS (fig. S33 and note S13). Figure 5E shows the representative dispersion curves acquired from the three positions. For continuous monitoring, the spectral analysis uses a shortened time window ($\Delta T = 0.5$ s) to boost temporal resolution, albeit at the cost of reduced spectral resolution (fig. S12). The experiment starts with the participant holding each posture for 10 s (cycle 1), followed by 6 cycles of bicep curls (movie S1). Each cycle progresses through the positions: 60°, 90°, 180°, 90°, and back to 60°. Figure 5F presents the raw z-axis acceleration data with the corresponding positions indicated. The automated algorithm, running on an external computer (Intel Core i7-12700KF CPU@3.61 GHz), outputs c_1 and c_2 in real time at a rate of 160 Hz (Fig. 5G). The sensor captures the continuous change in SWS. During the holding postures, the SWS transition from the initial relaxed state at 180° ($c_1 = 6.5 \pm 0.6$ m/s, $c_2 = 5.0 \pm 0.4$ m/s) to the loaded state at 90° ($c_1 = 9.7 \pm 0.8$ m/s, $c_2 = 9.5 \pm 0.8$ m/s) and to the intermediate relaxed state at 60° ($c_1 = 6.5 \pm 0.2$ m/s, $c_2 = 3.2 \pm 0.2$ m/s). For all cycles, the measured SWS peaks at the position ~135° during the transition from 180° to 90°. The estimated h_1 shows high correlation with c_1 and varies between 5 and 20 mm (fig. S31).

Testing across all 11 healthy participants demonstrates a similar trend in c_1 and c_2 during both weight-holding test and bicep-curl exercises (figs. S31 and S34 to S44 and note S14). These results validate the sensor's ability to reliably detect changes in muscle stiffness in real time and under ambulatory conditions across individuals.

DISCUSSION

This paper introduces MAW sensing, a wearable elastography technology designed for wireless, untethered measurement of subcutaneous tissue stiffness changes. The system's comprehensive hardware design, including soft sensor mechanics, ensures a robust skin-device interface that enables continuous, high-fidelity surface wave measurement, even in the presence of body deformation or motion artifacts. An automated algorithm using cross-power spectral analysis computes the dispersion relations of surface waves, which encode the mechanical properties of tissues at varying depths. FEA validated the experimentally measured dispersion relationships, while a nondimensional analysis based on FEA provides a mechanical model that correlates bilayer material stiffness, represented by SWS, with the detected surface wave speeds.

The resulting MAW sensing platform enables continuous, noninvasive monitoring of stiffness changes in soft materials and tissues. Tests on diverse phantoms demonstrate a bilayer stiffness measurement with estimation errors largely within 18%, covering a broad modulus range (in kilopascals to megapascals) with significant penetration depths of up to a few centimeters. Validation tests conducted on synthetic and porcine tissues show strong agreement between MAW and SWE measurements. The system effectively monitors the softening of porcine tissues following the PBS injection and the stiffening of human skeletal muscles under increasing load. Real-time assessments of bilayer stiffness in biceps during physical activities demonstrate the system's capability to continuously monitor relative stiffness changes in an ambulatory setting.

Compared to existing solutions (e.g., strain sensors, myotonometry, and ultrasound elastography), MAW offers distinct advantages including (i) wireless, low-power, and low-cost operation with no need for manual calibration; (ii) motion robustness via coherence filtering; and (iii) centimeter-scale depth resolution. These features make it uniquely suited for continuous or longitudinal monitoring of deep tissue stiffness in ambulatory settings (table S3), highlighting its potential for any applications that demand this capability.

The MAW sensor operates at a power consumption of 343 mW, comprising 33 mW from the sensor unit and 310 mW from the vibration actuator. This configuration supports up to 3 hours of continuous actuation and sensing. Building on engineering principles previously validated for long-term stability and biocompatibility (*50*–*52*), the sensor is expected to support extended-duration (>48 hours), stable, and safe wearable use. These results highlight the balance between accuracy, simplicity, and cost, showcasing its potential for tissue stiffness assessment in ambulatory environments without the need for expensive equipment or specialized personnel. Future enhancements include integrating a custom-designed, miniaturized actuator (*62*), optimized for actuation force and energy efficiency, and directly powered and controlled by the sensor's onboard battery and microcontroller. This will reduce overall power consumption and enhance the system's integrity and usability, especially in anatomically constrained areas. Expanding the system to incorporate a two-dimensional (2D) array of IMUs and exploring a multilayer mechanical model will enable 3D elastography with enhanced spatial resolution. Moreover, the MAW sensing platform has the potential to measure viscoelastic properties by analyzing both the phase velocity and wave attenuation across different frequencies, encompassing both storage and loss modulus. These capabilities could offer insights into conditions where tissue viscosity plays a crucial role, such as edema, tumor progression, muscle injuries, etc.

MATERIALS AND METHODS

Vibration actuator setup

A miniature speaker-type actuator (ASX02604-R, PUI Audio) was used to generate mechanical vibrations via a vertically oscillating diaphragm driven by a voice coil–magnet assembly. Power and control signals were supplied through a Bluetooth receiver (A3352, Anker), connected to the actuator via a 3.5-mm audio cable. The actuator and cable were enclosed in a custom-designed protective housing fabricated from 3D-printed acrylic, and the entire assembly was affixed to the skin using medical-grade double-sided silicone/acrylate adhesive (2477P, 3M). To minimize mechanical interference, both the receiver and cable were secured using soft silicone tape (V5000150, Medvance) at a flat anatomical site proximal to the actuator but spatially separated from the sensing region.

Ground-truth measurement of phantom materials

The Young's modulus was characterized by tensile tests (RSA G2, TA Instrument) under prescribed strains (<3%) at room temperature. The samples were cut into sizes of 20 mm by 5 mm by 1 mm (length by width by thickness) and fixed by a film tension clamp. Both loading and unloading strain rates are 5×10^{-4} s^{-1}. The error bars are SD from five tensile tests. The thickness of the phantom layers was measured using a caliper. The error bars are SD from 10 measurements.

Ultrasound B-mode imaging and SWE measurement

An operational frequency of 5.3 MHz was used for the SWE push excitation, and a track transmit frequency of 6.7 MHz was used for the measurements of SWS. The probe was fixed on a three-axis linear stage and positioned with the axial axis normal to the tissue surface, with ample ultrasound gel coupling, and maintained contact with minimal compression. SWS maps were placed and superimposed into ultrasound B-mode images for parallel comparison. One scan was taken for each SWE measurement. SD of the SWS acquired in the scanning region was used as the error bar to represent measurement uncertainty.

Human test protocols and specifications

Weight-holding and bicep-curl tests were conducted on 11 healthy participants (7 male and 4 female, aged 24 to 47). The weight-holding test was performed by a male participant seated in a chair, with the MAW sensor placed on the right bicep, holding 16 different weights

(0 to 4533 g) at a fixed elbow angle of 60°. For the cyclic lifting test, each participant lifted a 10-lb (4533 g; male) or 6-lb (2722 g; female) dumbbell while periodically changing the elbow angle (60°, 90°, and 180°). All human tests were approved by the Duke University Health System Institutional Review Board (protocol ID Pro00114164).

Supplementary Materials

The PDF file includes:

Note S1 to S14
Figs. S1 to S44
Tables S1 to S3
Appendix SI
Legend for movie S1

Other Supplementary Material for this manuscript includes the following:

Movie S1

REFERENCES AND NOTES

1. G. Singh, A. Chanda, Mechanical properties of whole-body soft human tissues: A review. *Biomed. Mater.* **16**, 062004 (2021).
2. A. M. Handorf, Y. Zhou, M. A. Halanski, W.-J. Li, Tissue stiffness dictates development, homeostasis, and disease progression. *Organogenesis* **11**, 1–15 (2015).
3. A. Massey, J. Stewart, C. Smith, C. Parvini, M. McCormick, K. Do, A. X. Cartagena-Rivera, Mechanical properties of human tumour tissues and their implications for cancer development. *Nat. Rev. Phys.* **6**, 269–282 (2024).
4. D. Englezos, C. Voutouri, T. Stylianopoulos, Machine learning analysis reveals tumor stiffness and hypoperfusion as biomarkers predictive of cancer treatment efficacy. *Transl. Oncol.* **44**, 101944 (2024).
5. D. R. Kwon, G. Y. Park, J. G. Kwon, The change of intrinsic stiffness in gastrocnemius after intensive rehabilitation with botulinum toxin A injection in spastic diplegic cerebral palsy. *Ann. Rehabil. Med.* **36**, 400–403 (2012).
6. D. Vasilescu, D. Vasilescu, S. Dudea, C. Botar-Jid, S. Sfrâgeu, D. Cosma, Sonoelastography contribution in cerebral palsy spasticity treatment assessment, preliminary report: A systematic review of the literature apropos of seven patients. *Med. Ultrason.* **12**, 306–310 (2010).
7. E. Song, Y. Huang, N. Huang, Y. Mei, X. Yu, J. A. Rogers, Recent advances in microsystem approaches for mechanical characterization of soft biological tissues. *Microsyst. Nanoeng.* **8**, 77 (2022).
8. K. Navindaran, J. S. Kang, K. Moon, Techniques for characterizing mechanical properties of soft tissues. *J. Mech. Behav. Biomed. Mater.* **138**, 105575 (2023).
9. Y. Yang, L. Qiu, L. Wang, X. Xiang, Y. Tang, H. Li, F. Yan, Quantitative assessment of skin stiffness using ultrasound shear wave elastography in systemic sclerosis. *Ultrasound Med. Biol.* **45**, 902–912 (2019).
10. C. Chen, Y. Cheng, X. Zhu, Y. Cai, Y. Xue, N. Kong, Y. Yu, D. Xuan, S. Zheng, X. Yang, Ultrasound assessment of skin thickness and stiffness: The correlation with histology and clinical score in systemic sclerosis. *Arthritis Res. Ther.* **22**, 197 (2020).
11. B. Müller, E. Mazza, C. Schiestl, J. Elrod, Longitudinal monitoring and prediction of long-term outcome of scar stiffness on pediatric patients. *Burns & Trauma* **9**, tkab028 (2021).
12. H. I. C. Harn, R. Ogawa, C. K. Hsu, M. W. Hughes, M. J. Tang, C. M. Chuong, The tension biology of wound healing. *Exp. Dermatol.* **28**, 464–471 (2019).
13. Z. Yu, N. Liu, L. Wang, J. Chen, L. Han, D. Sun, Assessment of skin properties in chronic lymphedema: Measurement of skin stiffness, percentage water content, and transepidermal water loss. *Lymphat. Res. Biol.* **18**, 212–218 (2020).
14. M. Sano, S. Hirakawa, Y. Yamanaka, E. Naruse, K. Inuzuka, T. Saito, K. Katahashi, T. Yata, T. Kayama, H. Tsuyuki, Development of a noninvasive skin evaluation method for lower limb lymphedema. *Lymphat. Res. Biol.* **18**, 7–15 (2020).
15. S. Park, A. L. Chien, I. D. Brown, J. Chen, Characterizing viscoelastic properties of human melanoma tissue using Prony series. *Front. Bioeng. Biotechnol.* **11**, 1162880 (2023).
16. C. M. Botar-Jid, R. Cosgarea, S. D. Bolboacă, S. C. Şenilă, L. M. Lenghel, L. Rogojan, S. M. Dudea, Assessment of cutaneous melanoma by use of very-high-frequency ultrasound and real-time elastography. *Am. J. Roentgenol.* **206**, 699–704 (2016).
17. B. K. Patel, K. Pepin, K. R. Brandt, G. L. Mazza, B. A. Pockaj, J. Chen, Y. Zhou, D. W. Northfelt, K. Anderson, J. M. Kling, C. M. Vachon, K. R. Swanson, M. Nikkhah, R. Ehman, Association of breast cancer risk, density, and stiffness: Global tissue stiffness on breast MR elastography (MRE). *Breast Cancer Res. Treat.* **194**, 79–89 (2022).
18. N. F. Boyd, Q. Li, O. Melnichouk, E. Huszti, L. J. Martin, A. Gunasekara, G. Mawdsley, M. J. Yaffe, S. Minkin, Evidence that breast tissue stiffness is associated with risk of breast cancer. *PLOS ONE* **9**, e100937 (2014).
19. J. M. Chang, I. A. Park, S. H. Lee, W. H. Kim, M. S. Bae, H. R. Koo, A. Yi, S. J. Kim, N. Cho, W. K. Moon, Stiffness of tumours measured by shear-wave elastography correlated with subtypes of breast cancer. *Eur. Radiol.* **23**, 2450–2458 (2013).
20. J. Marusiak, K. Kisiel-Sajewicz, A. Jaskólska, A. Jaskólski, Higher muscle passive stiffness in Parkinson's disease patients than in controls measured by myotonometry. *Arch. Phys. Med. Rehabil.* **91**, 800–802 (2010).
21. T. Rätsep, T. Asser, Changes in viscoelastic properties of skeletal muscles induced by subthalamic stimulation in patients with Parkinson's disease. *Clin. Biomech.* **26**, 213–217 (2011).
22. L.-l. Chuang, C.-y. Wu, K.-c. Lin, Reliability, validity, and responsiveness of myotonometric measurement of muscle tone, elasticity, and stiffness in patients with stroke. *Arch. Phys. Med. Rehabil.* **93**, 532–540 (2012).
23. S. Eby, H. Zhao, P. Song, B. J. Vareberg, R. Kinnick, J. F. Greenleaf, K.-N. An, S. Chen, A. W. Brown, Quantitative evaluation of passive muscle stiffness in chronic stroke. *Am. J. Phys. Med. Rehabil.* **95**, 899–910 (2016).
24. S. S. Lee, S. Spear, W. Z. Rymer, Quantifying changes in material properties of stroke-impaired muscle. *Clin. Biomech.* **30**, 269–275 (2015).
25. D. D. Aarrestad, M. D. Williams, S. C. Fehrer, E. Mikhailenok, C. T. Leonard, Intra-and interrater reliabilities of the myotonometer when assessing the spastic condition of children with cerebral palsy. *J. Child Neurol.* **19**, 894–901 (2004).
26. Å. Lidström, G. Ahlsten, H. Hirchfeld, S. Norrlin, Intrarater and interrater reliability of myotonometer measurements of muscle tone in children. *J. Child Neurol.* **24**, 267–274 (2009).
27. A. Boyaci, A. Tutoglu, N. Boyaci, I. Koca, M. Calik, A. Sakalar, N. Kilicaslan, Changes in spastic muscle stiffness after botulinum toxin A injections as part of rehabilitation therapy in patients with spastic cerebral palsy. *NeuroRehabilitation* **35**, 123–129 (2014).
28. M. Ditroilo, M. Watsford, E. Fernández-Peña, G. D'Amen, F. Lucertini, G. De Vito, Effects of fatigue on muscle stiffness and intermittent sprinting during cycling. *Med. Sci. Sports Exerc.* **43**, 837–845 (2011).
29. S. S. Banerjee, D. B. Krishnamani, P. A. Karthick, A. Arunachalakasi, R. Swaminathan, Influence of viscoelasticity on dynamic fatiguing behavior of muscle using myotonometry and surface electromyography measurements. *IEEE Trans. Instrum. Meas.* **71**, 1–9 (2022).
30. L. Lacourpaille, A. Nordez, F. Hug, V. Doguet, R. Andrade, G. Guilhem, Early detection of exercise-induced muscle damage using elastography. *Eur. J. Appl. Physiol.* **117**, 2047–2056 (2017).
31. X. Zhou, C. Wang, S. Qiu, L. Mao, F. Chen, S. Chen, Non-invasive assessment of changes in muscle injury by ultrasound shear wave elastography: An experimental study in contusion model. *Ultrasound Med. Biol.* **44**, 2759–2767 (2018).
32. J. T. Kalkhoven, M. L. Watsford, The relationship between mechanical stiffness and athletic performance markers in sub-elite footballers. *J. Sports Sci.* **36**, 1022–1029 (2018).
33. E. C. Pruyn, M. Watsford, A. Murphy, The relationship between lower-body stiffness and dynamic performance. *Appl. Physiol. Nutr. Metab.* **39**, 1144–1150 (2014).
34. J. M. McGowen, C. W. Hoppes, J. S. Forsse, S. R. Albin, J. Abt, S. L. Koppenhaver, The utility of myotonometry in musculoskeletal rehabilitation and human performance programming. *J. Athl. Train.* **58**, 305–318 (2023).
35. D. G. Schmitz, R. W. Nuckols, S. Lee, T. Akbas, K. Swaminathan, C. J. Walsh, D. G. Thelen, Modulation of Achilles tendon force with load carriage and exosuit assistance. *Sci. Robot.* **7**, eabq1514 (2022).
36. Z. S. Mahdian, H. Wang, M. I. M. Refai, G. Durandau, M. Sartori, M. K. MacLean, Tapping into skeletal muscle biomechanics for design and control of lower limb exoskeletons: A narrative review. *J. Appl. Biomech.* **39**, 318–333 (2023).
37. L. Aird, D. Samuel, M. Stokes, Quadriceps muscle tone, elasticity and stiffness in older males: Reliability and symmetry using the MyotonPRO. *Arch. Gerontol. Geriatr.* **55**, e31–e39 (2012).
38. S. Diridollou, F. Patat, F. Gens, L. Vaillant, D. Black, J. Lagarde, Y. Gall, M. Berson, In vivo model of the mechanical properties of the human skin under suction. *Skin Res. Technol.* **6**, 214–221 (2000).
39. R. Sanders, Torsional elasticity of human skin in vivo. *Pflugers Arch.* **342**, 255–260 (1973).
40. J.-L. Gennisson, T. Deffieux, M. Fink, M. Tanter, Ultrasound elastography: Principles and techniques. *Diagn. Interv. Imaging* **94**, 487–495 (2013).
41. E. Song, Z. Xie, W. Bai, H. Luan, B. Ji, X. Ning, Y. Xia, J. M. Baek, Y. Lee, R. Avila, H.-Y. Chen, J.-H. Kim, S. Madhvapathy, K. Yao, D. Li, J. Zhou, M. Han, S. M. Won, X. Zhang, D. J. Myers, Y. Mei, X. Guo, S. Xu, J.-K. Chang, X. Yu, Y. Huang, J. A. Rogers, Miniaturized electromechanical devices for the characterization of the biomechanics of deep tissue. *Nat. Biomed. Eng.* **5**, 759–771 (2021).
42. D. Gao, J. P. Lee, J. Chen, L. S. Tay, Y. Xin, K. Parida, M. W. M. Tan, P. Huang, K. H. Kong, P. S. Lee, A wearable pneumatic-piezoelectric system for quantitative assessment of skeletomuscular biomechanics. *Device* **2**, 100288 (2024).
43. Z. Cui, W. Wang, L. Guo, Z. Liu, P. Cai, Y. Cui, T. Wang, C. Wang, M. Zhu, Y. Zhou, W. Liu, Y. Zheng, G. Deng, C. Xu, X. Chen, Haptically quantifying Young's modulus of soft materials using a self-locked stretchable strain sensor. *Adv. Mater.* **34**, 2104078 (2021).

44. J. A. Martin, S. C. Brandon, E. M. Keuler, J. R. Hermus, A. C. Ehlers, D. J. Segalman, M. S. Allen, D. G. Thelen, Gauging force by tapping tendons. *Nat. Commun.* **9**, 1592 (2018).
45. H. Hu, Y. Ma, X. Gao, D. Song, M. Li, H. Huang, X. Qian, R. Wu, K. Shi, H. Ding, Stretchable ultrasonic arrays for the three-dimensional mapping of the modulus of deep tissue. *Nat. Biomed. Eng.* **7**, 1321–1334 (2023).
46. H.-C. Liu, Y. Zeng, C. Gong, X. Chen, P. Kijanka, J. Zhang, Y. Genyk, H. Tchelepi, C. Wang, Q. Zhou, X. Zhao, Wearable bioadhesive ultrasound shear wave elastography. *Sci. Adv.* **10**, eadk8426 (2024).
47. C. Dagdeviren, Y. Shi, P. Joe, R. Ghaffari, G. Balooch, K. Usgaonkar, O. Gur, P. L. Tran, J. R. Crosby, M. Meyer, Y. Su, R. Chad Webb, A. S. Tedesco, M. J. Slepian, Y. Huang, J. A. Rogers, Conformal piezoelectric systems for clinical and experimental characterization of soft tissue biomechanics. *Nat. Mater.* **14**, 728–736 (2015).
48. C. Wang, B. Qi, M. Lin, Z. Zhang, M. Makihata, B. Liu, S. Zhou, Y.-h. Huang, H. Hu, Y. Gu, Y. Chen, Y. Lei, T. Lee, S. Chien, K.-I. Jang, E. B. Kistler, S. Xu, Continuous monitoring of deep-tissue haemodynamics with stretchable ultrasonic phased arrays. *Nat. Biomed. Eng.* **5**, 749–758 (2021).
49. K. Lee, X. Ni, J. Y. Lee, H. Arafa, D. J. Pe, S. Xu, R. Avila, M. Irie, J. H. Lee, R. L. Easterlin, D. H. Kim, H. U. Chung, O. O. Olabisi, S. Getaneh, E. Chung, M. Hill, J. Bell, H. Jang, C. Liu, J. B. Park, J. Kim, S. B. Kim, S. Mehta, M. Pharr, A. Tzavelis, J. T. Reeder, I. Huang, Y. Deng, Z. Xie, C. R. Davies, Y. Huang, J. A. Rogers, Mechano-acoustic sensing of physiological processes and body motions via a soft wireless device placed at the suprasternal notch. *Nat. Biomed. Eng.* **4**, 148–158 (2020).
50. X. Ni, W. Ouyang, H. Jeong, J.-T. Kim, A. Tzaveils, A. Mirzazadeh, C. Wu, J. Y. Lee, M. Keller, C. K. Mummidisetty, Automated, multiparametric monitoring of respiratory biomarkers and vital signs in clinical and home settings for COVID-19 patients. *Proc. Natl. Acad. Sci. U.S.A.* **118**, e2026610118 (2021).
51. J.-Y. Yoo, S. Oh, W. Shalish, W.-Y. Maeng, E. Cerier, E. Jeanne, M.-K. Chung, S. Lv, Y. Wu, S. Yoo, A. Tzavelis, J. Trueb, M. Park, H. Jeong, E. Okunzuwa, S. Smilkova, G. Kim, J. Kim, G. Chung, Y. Park, A. Banks, S. Xu, G. M. Sant'Anna, D. E. Weese-Mayer, A. Bharat, J. A. Rogers, Wireless broadband acousto-mechanical sensing system for continuous physiological monitoring. *Nat. Med.* **29**, 3137–3148 (2023).
52. H. Jeong, J. Y. Lee, K. Lee, Y. J. Kang, J.-T. Kim, R. Avila, A. Tzavelis, J. Kim, H. Ryu, S. S. Kwak, Differential cardiopulmonary monitoring system for artifact-canceled physiological tracking of athletes, workers, and COVID-19 patients. *Sci. Adv.* **7**, eabg3092 (2021).
53. C. B. Park, R. D. Miller, J. Xia, Multichannel analysis of surface waves. *Geophysics* **64**, 800–808 (1999).
54. S. Yoon, G. J. Rix, Near-field effects on array-based surface wave methods with active sources. *J. Geotech. Geoenviron. Eng.* **135**, 399–406 (2009).
55. X. Feng, G.-Y. Li, A. Ramier, A. M. Eltony, S.-H. Yun, In vivo stiffness measurement of epidermis, dermis, and hypodermis using broadband Rayleigh-wave optical coherence elastography. *Acta Biomater.* **146**, 295–305 (2022).
56. M. Al-Hunaidi, Difficulties with phase spectrum unwrapping in spectral analysis of surface waves nondestructive testing of pavements. *Can. Geotech. J.* **29**, 506–511 (1992).
57. J. Achenbach, *Wave Propagation in Elastic Solids* (Elsevier, 2012).
58. G.-Y. Li, Y. Zheng, Y.-X. Jiang, Z. Zhang, Y. Cao, Guided wave elastography of layered soft tissues. *Acta Biomater.* **84**, 293–304 (2019).
59. L. Wang, F. Yan, Y. Yang, X. Xiang, L. Qiu, Quantitative assessment of skin stiffness in localized scleroderma using ultrasound shear-wave elastography. *Ultrasound Med. Biol.* **43**, 1339–1347 (2017).
60. J.-L. Gennisson, T. Deffieux, E. Macé, G. Montaldo, M. Fink, M. Tanter, Viscoelastic and anisotropic mechanical properties of in vivo muscle tissue assessed by supersonic shear imaging. *Ultrasound Med. Biol.* **36**, 789–801 (2010).
61. J. L. Gennisson, C. Cornu, S. Catheline, M. Fink, P. Portero, Human muscle hardness assessment during incremental isometric contraction using transient elastography. *J. Biomech.* **38**, 1543–1550 (2005).
62. X. Yu, Z. Xie, Y. Yu, J. Lee, A. Vazquez-Guardado, H. Luan, J. Ruban, X. Ning, A. Akhtar, D. Li, B. Ji, Y. Liu, R. Sun, J. Cao, Q. Huo, Y. Zhong, C. Lee, S. Kim, P. Gutruf, C. Zhang, Y. Xue, Q. Guo, A. Chempakasseril, P. Tian, W. Lu, J. Jeong, Y. Yu, J. Cornman, C. Tan, B. Kim, K. Lee, X. Feng, Y. Huang, J. A. Rogers, Skin-integrated wireless haptic interfaces for virtual and augmented reality. *Nature* **575**, 473–479 (2019).

Acknowledgments: We thank Duke University Shared Materials Instrumentation Facility, a member of the North Carolina Research Triangle Nanotechnology Network supported by the National Science Foundation (award no. ECCS-2025064) as part of the National Nanotechnology Coordinated Infrastructure, for the tensile testing. **Funding:** The work was supported by the National Institute of Biomedical Imaging and Bioengineering of the National Institutes of Health under award number R21EB034973. Additional support was provided by the National University of Singapore Presidential Young Professorship and the Ministry of Education, Singapore, under the Academic Research Fund Tier 1 (FY2023 and FY2024). **Author contributions:** Conceptualization: C.L., J.A.R., C.W., and X.N. Mechanical modeling and theoretical analysis: C.L., H.W., H.L., and Y.H. Embeded system and user interface: Z.S., Y.P., Z.Z., and W.D. Experiment: C.L., C.Q., K.Y., M.H., J.L., W.Y., S.C., H.S., T.-L.L., C.W., and X.N. Human participant study: Y.P., C.Q., K.Y., A.B.W., S.S.M.L., C.W., and X.N. Signal processing and data analysis: C.L. and X.N. Visualization: C.L., W.Z., and H.L. Supervision: J.A.R., C.W., and X.N. Writing—original draft: C.L., H.W., C.W., and X.N. Writing—review and editing: C.L., H.W., C.Q., K.Y., Y.H., J.A.R., C.W., and X.N. **Competing interests:** X.N., J.A.R., C.W., and C.L. are inventors on a published, pending patent application related to this work, filed by Northwestern University and Duke University (US20240108279A1, published on 4 April 2024). The other authors declare that they have no competing interests. **Data and materials availability:** All data needed to evaluate the conclusions in the paper are present in the paper and/or the Supplementary Materials. Source data for figures are available from figshare with the identifier https://doi.org/10.6084/m9.figshare.28673879.

Submitted 9 April 2025
Accepted 6 August 2025
Published 3 September 2025
10.1126/sciadv.ady0534

Science Advances

Wireless, wearable elastography via mechano-acoustic wave sensing for ambulatory monitoring of tissue stiffness

Chenhang Li, Heling Wang, Ziwu Song, Wei Zhang, Yuxin Pan, Zihao Zhao, Chaorui Qiu, Kaiping Yin, Mengdi Han, Allison Bingqing Wang, Haiwen Luan, Jiahong Li, Wenyuan Yan, Shulin Chen, Haixu Shen, Tzu-Li Liu, Sabrina S. M. Lee, Wenbo Ding, Yonggang Huang, John A. Rogers, Changsheng Wu, and Xiaoyue Ni

Sci. Adv. **11** (36), eady0534. DOI: 10.1126/sciadv.ady0534

Science Advances (ISSN 2375-2548) is published by the American Association for the Advancement of Science. 1200 New York Avenue NW, Washington, DC 20005. The title *Science Advances* is a registered trademark of AAAS.